

Optically controlled optical gate with an optoelectronic dual diode structure – theory and experiment

M. B. YAIRI*, H. V. DEMIR AND D. A. B. MILLER
Stanford University, Stanford, CA 94305, USA
(*author for correspondence)

Received 10 August 2000; accepted 23 October 2000

Abstract. A low-power, surface-normal optically controlled optical gate that incorporates two stacked AlGaAs diodes has been tested using both picosecond and femtosecond pulses. The device opens and closes within 20 ps with a 30% reflectivity change. Repeated gating with 20 ps periods has been demonstrated – a repetition period significantly faster than the external RC time constant. A theory of the dynamics of optically induced voltage across multiple-layered structures is presented and has been incorporated into simulations, matching experimental results well. This theory also provides insight into both the form and possible improvement of the device recovery using multiple layers.

Key words: optical gate, all-optical switches

1. Introduction

The ability to manipulate optical data on a bit-by-bit level with light instead of electronics is of strategic importance for future data networks, and over the past two decades a variety of different types of all-optical switches has been developed (Stegeman and Miller 1993). Many such switches are waveguide based: a waveguide keeps the optical intensity high while at the same time limiting the area over which a change must be made in order to manipulate the light. In fiber waveguides, one of the first such devices studied was the non-linear all-optical loop mirror (Doran and Wood 1988), based on interference of counter-propagating light beams. The low $\chi^{(3)}$ of fused silica glass requires long fiber lengths and high intensity light. Soliton gates are also pure fiber devices although they operate on entirely different principles (Islam 1989; Islam *et al.* 1990, 1992; Islam and Soccoloch 1991). They, too, suffer from length and intensity limitations (though this is improving) but have the advantages of fast switching and fast system recovery. To avoid relying on the low $\chi^{(3)}$ of fiber for switching, semiconductor optical amplifiers have been integrated with fiber systems. These devices, such as the terahertz optical asymmetric demultiplexer (Sololoff *et al.* 1993), semiconductor laser

amplifier in an optical loop mirror (Eiselt 1992), and their refinements (Ellis and Spritir 1993; Eiselt *et al.* 1995; Ahn *et al.* 1997; Mannin *et al.* 1997), have lower switching energy requirements and may be made using shorter lengths of fiber as well. However, such hybrids have the disadvantage of somewhat awkward integration of fiber (on the order of meters) and semiconductor waveguide devices. Numerous purely semiconductor waveguide switches, usually based on photogenerated carrier effects, have also been extensively researched, including the well-known non-linear directional coupler (Likamwa *et al.* 1986, 1990; Aitchison *et al.* 1991) among others (Gontijo *et al.* 1996; Campi *et al.* 1998; Leuthold *et al.* 1998). As a group, semiconductor waveguides generally have the advantage of small size and low switching power, but relatively slow recovery rates for high-repetition devices. Some switches not limited by carrier lifetimes include those based on the optical Stark effect (Paye and Hulin 1993; Kan'an *et al.* 1996) – which is fast but requires relatively large light intensities – or parametric processes using $\chi^{(2)}$ in ferroelectrics which can exhibit low-switching energy in compact devices (Yokohama *et al.* 1997; Parameswaran *et al.* 2000).

All-optical switches have also been made which use light traveling at normal incidence to the semiconductor surface as opposed to running along a length of semiconductor as in a waveguide. The interaction length of these surface-normal devices is usually on the order of a few microns as compared to hundreds of microns or more in a waveguide, therefore strong intensity-dependent behavior is required for switching to occur. Devices based on absorption saturation have been developed that have good contrast ratios and high-repetition rates (Takahashi *et al.* 1996; Kobayashi *et al.* 1998; Loka and Smith 2000). Since they are surface-normal, they are not only much smaller than waveguide devices but are easily scalable in two dimensions to $N \times N$ formats. Moreover, they can also avoid the tight alignment requirements of waveguide devices. The required switching energy, however, is relatively large and, because they are absorption-based devices, they are difficult to efficiently cascade (as opposed to some waveguide switches based on, for example, refractive index changes or soliton interactions).

Unlike all of these devices, the optically controlled optical gate (OCOG) we present here switches a beam of light by inducing a local change in voltage across the device, much like an electrically controlled optical switch commonly does. Neither a light-field induced index change nor a band-filling effect due to the creation of charge carriers is involved. Integrating multiple quantum wells (MQWs) into the structure allows us to operate the device based on the quantum confined Stark effect (QCSE) (Miller *et al.* 1985). It is already well known that this effect, combined with optical detection, can make devices with large effective optical non-linearities and switches with low required optical energy densities. These properties are exploited in self-electrooptic-effect devices (SEEDs) (Miller 1990; Lentine and Miller 1993).

(Indeed, the present device with photodetection controlling electroabsorption, could be viewed as a member of the SEED family of devices.)

Our device also operates with surface-normal pulses but requires only about one-fifth to one-tenth of the switching energy compared to Takahashi *et al.* (1996), Kobayashi *et al.* (1998) and Loka and Smith (2000), although its contrast ratio is smaller. Moreover, because our device is inherently optoelectronic, it may be easily integrated with CMOS using flip-chip bonding (Goossen *et al.* 1995). It is important to note that, unlike most all-optical switches, this device can also independently electrically control the optical switch at speeds important for telecommunications, and its optoelectronic nature potentially allows for a wide variety of novel applications, including simultaneous switching and data monitoring.

The work in this paper shows an OCOG operated with multiple successive pulses, demonstrating burst logic rates with a 50 GHz clock speed. An optical gate such as this might be useful in multiplexing and demultiplexing data streams or as a gated sampler in analog-to-digital conversion systems. The remainder of this paper is organized as follows: the basic operation is described in Section 2; Section 3 outlines the specific device design and testing methods. Both simulation and experimental results are presented in Section 4, a more detailed description of the theory governing device recovery is given in Section 5 followed by a discussion of the effects of multiple-layered devices in Section 6 and conclusions in Section 7.

2. Description of device behavior

This OCOG is composed of two p-i-n diodes on top of a distributed Bragg reflector (DBR) mirror (Fig. 1). The bottom (modulator) diode, which contains MQWs in its intrinsic region, has its absorption switched when an incident control pulse is absorbed in the top (control) diode.

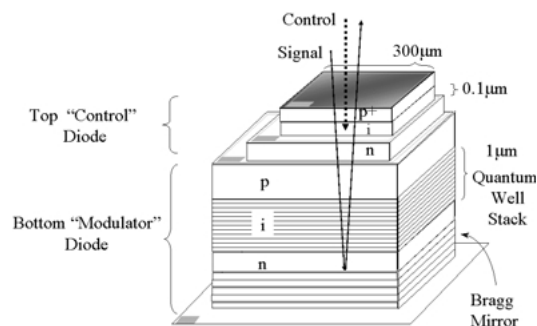


Fig. 1. Device schematic of a double diode structure with an ITO deposition over a thin top diode (100 nm intrinsic region) and a p-i(MQW)-n bottom diode.

The control diode, operated under reverse bias, is designed to be transparent to the signal (probe) pulse, but opaque to the control (pump) pulse, which is at a shorter wavelength. The modulator diode is only slightly reverse-biased so that the MQWs are initially substantially transparent to the signal compared to when the gate is 'on'; the system is in its highly reflective state for the signal. Upon absorption of the control pulse in the top diode, the photogenerated carriers vertically separate, locally screening the reverse bias across the top diode in the vicinity of the control pulse spot. As a consequence of the dual diode structure, the reverse bias voltage on the bottom diode is locally increased, raising the absorption of the MQWs – and hence decreasing the reflectivity of the device – through the QCSE. The 'turn-on' time of the device is determined by the voltage build-up time due to carrier transport in the intrinsic region of the top diode. The 'turn-off' time of the device is controlled by the local electrical relaxation of the voltage across the diodes through diffusive conduction (Livescu *et al.* 1989), operating on a picosecond time scale and described in detail in Section 3. The device repetition rate is limited by this fast on–off cycle rather than the external RC time constants.

A previous generation of this device, designed with a single p–i(MQW)–n diode (Yairi *et al.* 1999), was limited by the escape times of the photogenerated carriers (principally holes) from the quantum wells as well as by the drift time required to reach the doped layers. By separating the control and modulation functions, it is possible to optimize each separately. Using a bulk intrinsic region in the top diode avoids limits due to carrier escape times and also allows for potentially thinner regions and hence shorter transit times. A key aspect of the dual diode device is that its top-most and bottom-most regions are highly conducting with respect to the middle. As a consequence, every point in the lateral plane of one of these two layers is effectively held at a nearly constant voltage with respect to its opposite point in the other layer. Therefore, any local voltage reduction in the top diode leads to a corresponding local voltage increase in the bottom diode.

3. Design and testing

The OCOG is a molecular beam epitaxy grown AlGaAs structure, as has been previously described by Yairi *et al.* (1999). It consists of a top p–i–n diode and a bottom p–i(MQW)–n diode on the top of a DBR stack centered at 850 nm. The topmost p- and intrinsic-layers are only 50 and 100 nm thick, respectively, including a GaAs capping layer. Except for the bottom diode's intrinsic region and the DBR mirror, all other layers are Al_{0.3}Ga_{0.7}As. To increase the conductivity of the top p-layer, 660 nm of indium-tin-oxide

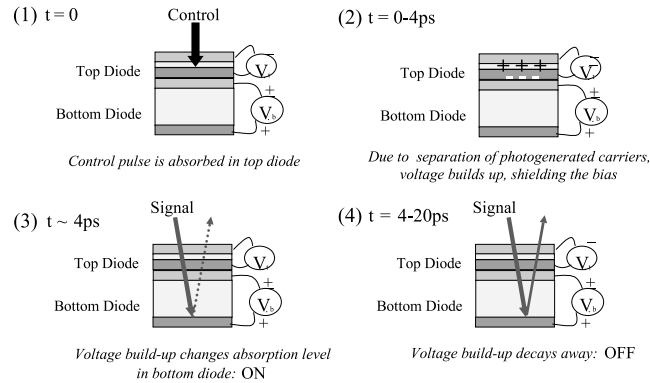


Fig. 2. Schematic of the OCOG device operation with picosecond pulses.

(ITO) was deposited; this layer also acts as an anti-reflection coating.¹ Device processing produced square mesas $300\ \mu\text{m}$ wide on a side with wire bonds to each of the four conducting layers of the double-diode structure.

A TsunamiTM Ti-Sapphire laser operating at 82 MHz was used to generate both 2 ps and 100 fs pulses. A standard pump-probe setup was used for testing with a BBO crystal (1 mm thick) to frequency double the pump.

To test the device's response to multiple optical pulses, a stream of four control pulses was generated and focused on the device. Creating such a pulse stream was accomplished using a large beam splitter ($5 \times 5\text{cm}^2$) and four corner cubes, one on each side of the beam splitter. Through careful realignment of the multiple retroreflections, the original pulse was split and recombined three times with a final result of eight beams (two groups of four), half of which went to a beam dump and the other half of which exited the beam splitter spatially overlapped. By varying the individual corner cubes' distances from the beam splitter, it was possible to control the relative time delay of each pulse with respect to the others. Because of the multiple splittings and reflections involved in creating the pulse stream, the final power in each pulse was limited to the small signal regime ($\sim 70\ \text{fJ/pulse}$).

4. Results

In this section we present both simulation and experimental results. For small signal simulations, the diffusive conduction response is calculated by the

¹ The ITO we used was 75% absorbing instead of an expected 5-10%. We believe this was due to processing difficulties and not inherent to the device operation. Consequently, in this paper we discount the ITO absorption in reflectivity and power calculations.

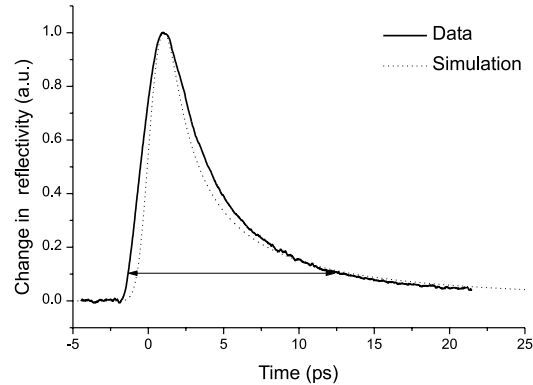


Fig. 3. Small signal (70 fJ/pulse) response data and simulation of the optical gate with 100 fs control and signal pulses and spot size of 5 μm , demonstrating 13 ps full-width 10% maximum (horizontal, arrowed line) turn on–off time.

method described in Section 5 below using the parameters of resistance per square and capacitance per unit area provided. The result is then convolved with the control pulse length and the carrier drift behavior in the top diode (modeled separately) to determine the overall reflectivity response of the device. Finally, the result is convolved with the signal (probe) pulse length to determine the output as seen by the photodetector. This approach is similar to the Green's function methodology used elsewhere (Yang *et al.* 1997).

Small signal (70 fJ switching energy) response of the device was tested using a 428 nm control pulse and a 857 nm signal pulse; the top diode was biased at 4.0 V and the bottom diode biased at -2.7 V. With a 5 μm spot radius and 100 fs pulses, the full-width at 10% maximum gating time was 13 ps (Fig. 3), while it was also 13 ps (Fig. 4) for 2 ps pulses with a spot size of 3.5 μm . The theoretical simulations of the device response are in good agreement with both sets of experimental data (i.e. both for δ -like pulses and extended pulses in time), verifying the validity of our model. The switching time presented here includes the effect of the finite pulse length of the read-out (signal) pulse. If the read-out pulse is deconvolved from the results, the actual length of the time the gate is 'on' is just 10 ps (using the pulse length and spot size given in Fig. 4).

Large signal device behavior is presented in Fig. 5. The spot size radius was again 3.5 μm , while the switching energy was 1.5 pJ (39 fJ/ μm^2) using 2 ps pulses. Excluding the parasitic absorption of the ITO (described above) and the top p-layer, approximately a 2-to-1 contrast ratio was achieved with a change in absolute reflectivity of about 30%. The optical gate opens and closes – returns to 10% of maximum change – within 20 ps; it is 17 ps when the read-out pulse is deconvolved from the data.

The slightly slower response compared to small signal behavior likely stems from the carriers fully screening the reverse bias across the top diode

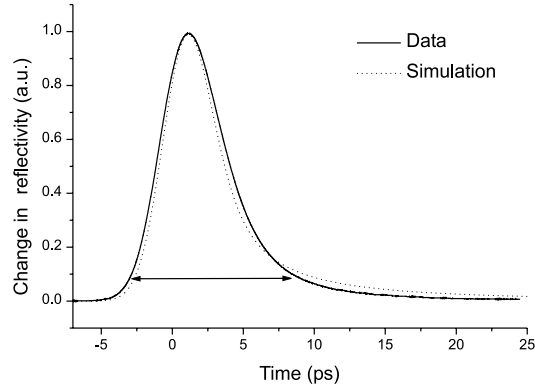


Fig. 4. Small signal response data and simulation of the optical gate with 2 ps control and signal pulses and spot size of $3.5 \mu\text{m}$, demonstrating 13 ps full-width 10% maximum (horizontal, arrowed line) turn on-off time.

before they reach the doped layers, slowing vertical carrier transport. This is demonstrated more clearly in Fig. 6(a). As the power of the control pulse rises the normalized device response stays constant until a critical value is reached. Beyond that limit, the turn-off time significantly increases. As the voltage applied across the top diode decreases, making it easier to be fully shielded, the magnitude of this critical power also decreases, as expected. Moreover, as Fig. 6(b) shows, as the power increases, the turn-on time decreases, indicating that when more carriers are created the carriers do not need to move as far to produce a given voltage shift (and that this shift is limited by the top diode reverse bias).

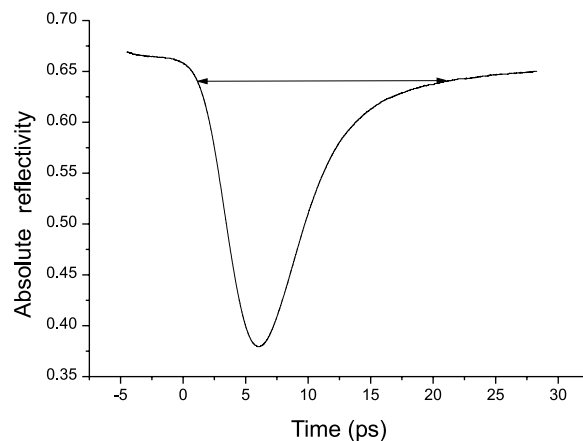


Fig. 5. Large signal response of the optical gate with 2 ps control and signal pulses and spot size of $3.5 \mu\text{m}$, demonstrating 20 ps full-width 10% maximum (horizontal, arrowed line) turn on-off time with a 30% reflectivity change.

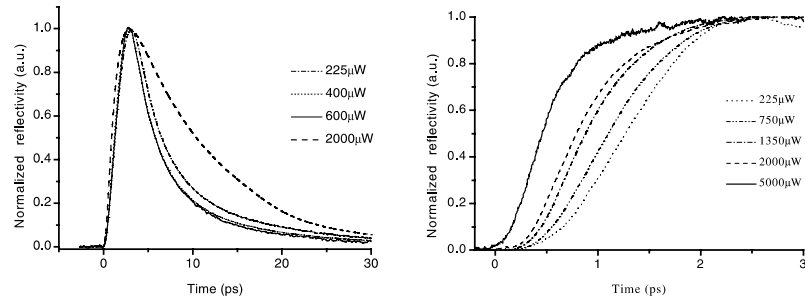


Fig. 6. Overall (a, left) and initial (b, right) device response at a various input powers of a 100 fs, 5 μm radius pulse, with the top diode biased at -8.0 V (left), and 1.0 V (right).

Fig. 7 shows the device's response to four control pulses, each separated by 20 ps. Simulation results match well, with the discrepancy likely due to imperfect matching of the pulse energies in the pulse stream generator. This key result – the ability of the device to recover in a short time limited only by the fast diffusive conduction response, not the external RC time constants – is clearly evident. There is a slight increase in the base reflectivity level for the later pulses due to the build-up of the decay of the previous pulses. Simulations show that this build-up of base reflectivity (critical if the device is to be used as a modulator at these rates) levels off to a manageable level not far from what is already seen here.

5. Theory of multilayer diffusive conduction

We have developed a model of the voltage behavior of OCOG multilayer structures in which a set of coupled differential equations governs the voltage

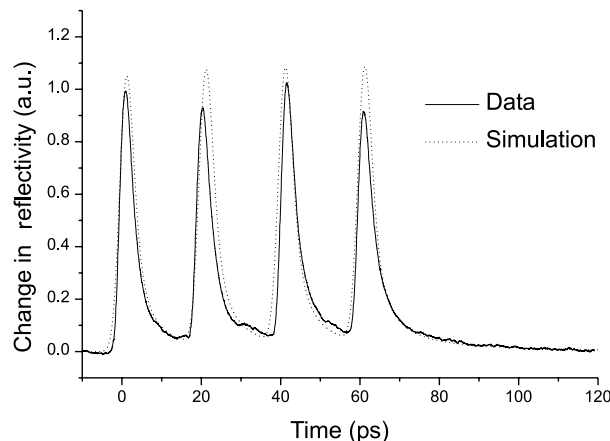


Fig. 7. Multiple-pulse, small signal response of the optical gate with 20 ps pulse separation.

dynamics across each dielectric layer. Given the initial conditions set by the photogenerated carriers, the non-uniform voltage build-up laterally diffuses away through diffusive conduction, turning the gate 'off'.

Diffusive conduction, sometimes referred to as enhanced diffusion, was first described by Livescu *et al.* (1989). This mechanism has since been used as the basis for optically controlled modulation and sampling by several groups (Schneider *et al.* 1992; Bradley *et al.* 1996; Yang *et al.* 1997). The diffusive conduction mechanism appears to be very closely related to the mechanism called giant ambipolar diffusion by some other authors, which has also been extensively studied (Dohler 1986; Gulden *et al.* 1991; Poole *et al.* 1993; Streb *et al.* 1999).

A vertically grown p-i-n diode can be viewed as a sandwich of capacitance per unit area of the intrinsic region between the slightly resistive planes of the p and n regions, each with a resistance per square determined by their doping level and thickness. A localized voltage build-up across the intrinsic region relaxes via diffusive conduction, smoothing itself out across the device. Equivalently, the voltage decays through lossy electromagnetic wave propagation.

A familiar manifestation of this phenomenon is signal propagation along a one-dimensional (1D) RC line (see Fig. 8(a)). A voltage pulse travels along the line determined by a diffusion coefficient proportional to its RC time constant, often much more quickly than an individual electron may move on average. The equations which describe the voltage are

$$-\frac{dV}{dx} = IR \quad (1)$$

and

$$\frac{dV}{dt} = -\frac{1}{C} \frac{dI}{dx} \quad (2)$$

Together, these equations provide a complete description of the voltage dynamics in the form of a diffusion equation:

$$\frac{dV}{dt} = \frac{1}{RC} \frac{\partial^2 V}{\partial x^2} = D \nabla_x^2 V \quad (3)$$

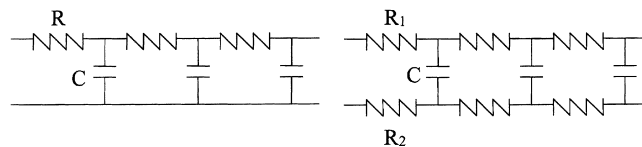


Fig. 8. Schematic of 1D RC transmission line with a single (a, left) or with two resistive planes (b, right).

where D is the diffusion coefficient. For two resistors (Fig. 8(b)), effective resistance given by their sum:

$$D = \frac{1}{R_{\text{effective}}C} = \frac{1}{(R_1 + R_2)C} \quad (4)$$

A p-i-n diode is the two-dimensional analog of the 1D case with characteristic equation

$$\frac{dV}{dt} = D\nabla_r^2 V \quad (5)$$

The only difference is that now the resistance and capacitance are given per unit area instead of per unit length: $D = 1/R_{\text{sq}}C_{\text{area}}$, where R_{sq} is the sum of the resistance per square of the p- and n-layers and the capacitance per unit area is determined by the thickness of the intrinsic layer. As a result, the diffusion coefficient is controllable via doping and growth parameters. If an instantaneous surface-normal light pulse is spatially gaussian, $V(r, t = 0)$ is given by:

$$V(r, t = 0) = V_M \exp\left(\frac{-r^2}{w_0^2/2}\right), \quad V_M \equiv \frac{Q_{\text{TOT}}}{C_A \pi \left(\frac{w_0}{\sqrt{2}}\right)^2} \quad (6)$$

Here Q_{TOT} is the total photogenerated charge and w_0 is the spot size radius. An analytic solution to Equation (5) is then given by

$$V(r, t) = V_M \left(\frac{\tau}{t + \tau}\right) \exp\left(\frac{-r^2}{4D(t + \tau)}\right), \quad \tau \equiv \left(\frac{w_0}{\sqrt{2}}\right)^2 \frac{1}{4D} \quad (7)$$

When $r=0$, $V(r=0, t)$ simplifies to a constant times a decay of $\tau/(t + \tau)$, sometimes referred to as a hyperbolic decay. The falls more quickly than an exponential decay for small t , and more slowly for large t .

The voltage behavior becomes more complicated when a multiple layer structure is considered, where ‘layer’ refers to a plane of capacitors sandwiched by resistors. A two-layer structure is shown in Fig. 9. The voltage across any particular layer is coupled to all of the resistances and capacitances of the entire structure, hence the analysis is more involved.

To tackle this problem, we first find the coupled partial differential equations governing voltage for the system. The equations are re-expressed in an eigenvector basis for which analytic solutions are known. Finally, the dynamics of the original voltages are expressed as a weighted sum of the eigenvectors. This process is explored in more detail below.

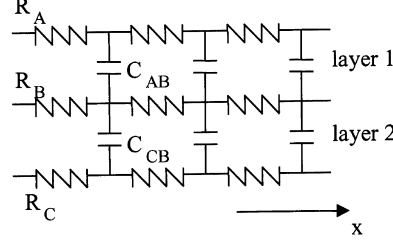


Fig. 9. Schematic of two-layer 1D RC structure.

For the two-layer structure, we may write (using Ohm's law)

$$\begin{aligned} \frac{-dV_A}{dx} &= V_A - V_{A'} = I_A R_A, & \frac{-dV_C}{dx} &= V_C - V_{C'} = I_C R_C, \\ \frac{-dV_B}{dx} &= V_B - V_{B'} = I_B R_B \end{aligned} \quad (8)$$

Kirchoff's equations provide the relationships

$$\frac{dI_A}{dx} = -I_{AB}, \quad \frac{dI_C}{dx} = -I_{CB}, \quad \frac{dI_B}{dx} = I_{AB} + I_{CB} \quad (9)$$

and, using $\{Q = CV\} \partial/\partial t$,

$$\frac{((-dI_A)/dx)}{C_{AB}} = \frac{I_{AB}}{C_{AB}} = \frac{dV_{AB}}{dt}, \quad \frac{((-dI_C)/dx)}{C_{CB}} = \frac{I_{CB}}{C_{CB}} = \frac{dV_{CB}}{dt} \quad (10)$$

In the above equations, subscripts A, B, and C refer to the top, middle, and bottom resistive planes, respectively, while subscripts AB and CB refer to currents and voltages across layer 1 and layer 2, respectively. These equations may be combined (e.g. taking the derivative with respect to 'x' of Equation (8) and combining with Equation (9) to substitute for I_A, I_B , and I_C in Equation (10) so that they reduce to two coupled equations in terms of the voltages of interest:

$$\frac{\partial V_{AB}}{\partial t} = D_A \left\{ \frac{\partial^2 V_{AB}}{\partial x^2} - \frac{\partial^2 V_{CB}}{\partial x^2} \phi_C \right\}, \quad \frac{\partial V_{CB}}{\partial t} = D_C \left\{ \frac{\partial^2 V_{CB}}{\partial x^2} - \frac{\partial^2 V_{AB}}{\partial x^2} \phi_A \right\} \quad (11)$$

where

$$\phi_A \equiv \frac{R_B}{R_B + R_A}, \quad \phi_C \equiv \frac{R_B}{R_B + R_C}$$

$$D_A \equiv \frac{1}{C_{AB}} \frac{1}{(R_A + R_C \phi_C)}, \quad D_C \equiv \frac{1}{C_{CB}} \frac{1}{(R_C + R_A \phi_A)}$$

Although we have written these expressions in terms of 1D equations, the general form holds for two dimensions as well.

It is worth examining the coupling relationship suggested by Equation (11). The coupling strength of the second diode is determined by the relative magnitude of the middle resistive layer, which acts as a voltage divider. As this resistance drops, the middle plane becomes conducting, isolating the voltage behavior of one layer from the other. Conversely, as the resistance in the middle rises, the coupling increases until ultimately the device functions as if it contained only a single intrinsic region with an effective capacitance of C_{AB} and C_{CB} in series.

We can rewrite the coupled equations in a matrix form

$$\frac{d}{dt} \tilde{U} = \tilde{D} \nabla_r^2 \tilde{U} \quad (12)$$

where

$$\tilde{U} = \begin{pmatrix} V_{AB} \\ V_{CB} \end{pmatrix}, \quad \tilde{D} = \begin{pmatrix} D_{11} & D_{12} \\ D_{21} & D_{22} \end{pmatrix} = \begin{pmatrix} \frac{1}{C_{AB}} \frac{1}{(R_A + R_C \phi_C)} & \frac{-1}{C_{AB}} \frac{\phi_C}{(R_A + R_C \phi_C)} \\ \frac{-1}{C_{CB}} \frac{\phi_A}{(R_C + R_A \phi_A)} & \frac{1}{C_{CB}} \frac{1}{(R_C + R_A \phi_A)} \end{pmatrix} \quad (13)$$

To decouple these equations, the eigenvalues $\tilde{\lambda}$ and eigenvectors $\tilde{\varphi}$ of \tilde{D} are determined, from which the transformation matrix \tilde{S} is found, relating the eigenvectors to the original voltages, \tilde{U} .

$$\tilde{U} = \tilde{S} \tilde{\varphi}, \quad \tilde{S} = \begin{pmatrix} -D_{12} & -D_{12} \\ D_{11} - \lambda_+ & D_{11} - \lambda_- \end{pmatrix} \quad (14)$$

Next, the initial voltage conditions are transformed into the eigenvector basis:

$$\tilde{\varphi}_0 = \tilde{S}^{-1} \tilde{U}_0 \quad (15)$$

Hence, we may now write decoupled differential equations in which the diffusion coefficients are simply the eigenvalues.

$$\frac{\partial}{\partial t} \tilde{\varphi} = \tilde{\lambda} \nabla^2 \tilde{\varphi} \quad (16)$$

where $\tilde{\lambda}$ is a diagonal matrix of the eigenvalues. It is therefore possible to solve for a particular eigenvector ('eigen-voltage') $\varphi(r, t)$ using the known

solutions to the uncoupled diffusion equation. Finally, these solutions may be transformed back into the original basis set, providing the full dynamic response of the system:

$$\tilde{U}(r, t) = \tilde{S} \tilde{\varphi}(r, t) \quad (17)$$

As an example, if our initial condition is a gaussian voltage distribution across the first layer with no voltage across the bottom layer (this happens if a short pulse of light is absorbed in the top diode and the photogenerated carriers are whisked rapidly to the p- and n- layers, as occurs in the OCOG described in this paper), we have

$$\tilde{U}_0 = \begin{pmatrix} V_0 \\ 0 \end{pmatrix} \quad (18)$$

$$\tilde{\varphi}_0 = \begin{pmatrix} \varphi_{+0} \\ \varphi_{-0} \end{pmatrix} = \frac{V_0}{(1/(D_A - \lambda_+) - 1/(D_A - \lambda_-))} \begin{pmatrix} 1 \\ 0 \end{pmatrix} \quad (19)$$

where

$$\lambda_{\pm} = \frac{D_{22} + D_{11} \pm \sqrt{(D_{22} + D_{11})^2 - 4(D_{22}D_{11} - D_{12}D_{21})}}{2} \quad (20)$$

(see Equation (13) for a description of D_{ij}). Using the decoupled solution to the diffusion equation given a gaussian distribution (Equation (7)),

$$\tilde{\varphi}_{\pm}(r, t) = \frac{\pm V_0}{(1/(D_A - \lambda_+) - 1/(D_A - \lambda_-))} \frac{\tau_{\pm}}{t + \tau_{\pm}} \exp\left(\frac{-r^2}{4\lambda_{\pm}(t + \tau_{\pm})}\right) \quad (21)$$

and Equation (17),

$$\tilde{U}(r, t) = \begin{pmatrix} V_{AB}(r, t) \\ V_{CB}(r, t) \end{pmatrix} = \begin{pmatrix} \frac{1}{D_A - \lambda_+} & \frac{1}{D_A - \lambda_-} \\ \frac{1}{D_A \phi_A} & \frac{1}{D_A \phi_A} \end{pmatrix} \begin{pmatrix} \varphi_+(r, t) \\ \varphi_-(r, t) \end{pmatrix} \quad (22)$$

we find that at the center of the pulse ($r = 0$) the voltages are given by

$$\begin{pmatrix} V_{AB}(r = 0, t) \\ V_{CB}(r = 0, t) \end{pmatrix} = \begin{pmatrix} \frac{V_0}{\left(1 - \frac{D_A - \lambda_+}{D_A - \lambda_-}\right)} \frac{\tau_+}{t + \tau_+} - \frac{V_0}{\left(\frac{D_A - \lambda_-}{D_A - \lambda_+} - 1\right)} \frac{\tau_-}{t + \tau_-} \\ \frac{V_0}{D_A \phi_A} \frac{1}{\left(\frac{1}{D_A - \lambda_+} - \frac{1}{D_A - \lambda_-}\right)} \left(\frac{\tau_+}{t + \tau_+} - \frac{\tau_-}{t + \tau_-}\right) \end{pmatrix} \quad (23)$$

Looking carefully at this result, we see that the voltage dynamics are governed by two eigenvalue diffusive time constants, τ_+ and τ_- . If R_A and $R_C \ll R_B$, τ_+ is very small compared to τ_- . The voltage across the bottom diode, V_{CB} , at first grows at a rate primarily determined by τ_- , while V_{AB} falls equally fast. After this increase, both V_{CB} and V_{AB} decay at the (slower) rate determined by τ_- . This is shown in Fig. 10, validating our more approximate original statement that highly conducting top-most and bottom-most layers ‘hold the voltage constant across the device,’ and the subsequent implication that the voltage of the bottom diode mimics the opposite behavior of the top diode.

The analysis described above may be extended in a straightforward manner to describe the voltage dynamics of a device with an arbitrary number of layers. This general approach is composed of four steps: (1) determine the coupling diffusion matrix \tilde{D} ; (2) solve the eigenvector problem to describe a decoupled system; (3) apply the solution to the regular (uncoupled) diffusion equation for the eigenvectors; (4) transform the dynamic solution back to the original variables. Steps (2)–(4) are identical to those just described. All that is left to do is determine the original coupling matrix, \tilde{D} . The Appendix describes this process in more detail. The key result is that the voltage obeys a diffusion equation

$$\frac{\partial}{\partial t} \tilde{V} = \tilde{D} \nabla^2 \tilde{V} \quad (24)$$

where \tilde{D} may be determined from the following relationship

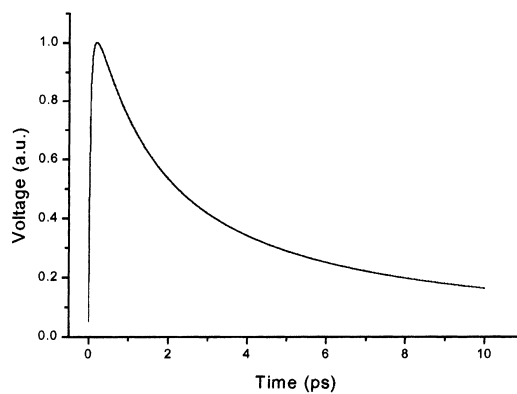


Fig. 10. Bottom diode voltage behavior ($-V_{CB}$) at pulse center ($r = 0$). Note the two separate behaviors: a very fast rise time (hence voltage across entire device essentially kept constant) and a slower fall time due to an impulse voltage on the top diode. Specific parameters used are $\tilde{C} = [6.67, 15.8, 1.0]$ $0.1 \text{ fF}/\mu\text{m}^2$, $\tilde{R} = [20, 300, 2000, 25]$ ohms per square, and spot size radius $3.5 \mu\text{m}$.

$$\tilde{D} = \frac{1}{\tilde{C}} \tilde{M}_{1[M]}^{-1} \frac{1}{\tilde{R}_{[M]}} \tilde{M}_{2[M]}^{-1} \quad (25)$$

The division of \tilde{R} (a vector related to the resistance per square of each resistive plane) and \tilde{C} (the capacitance per unit area of each layer) mean element-by-element operations instead of matrix operations, and $\tilde{M}_{1[M]}^{-1}$ and $\tilde{M}_{2[M]}^{-1}$ are determined simply by the number of layers. From this point forward the method described earlier in this section for determining the voltage dynamics using eigenvalues and eigenvectors becomes straightforward to apply.

6. Discussion

Does the presence of extra layers help or hinder device operation? One might suggest that adding extra layers simply presents extra resistance and capacitance, reducing device speed. This is not the case. In fact, increasing the number of layers significantly improves device speed. The dual diode (p-i-n-p-i-n) structure actually contains three depletion regions: two intrinsic regions in the top and bottom diodes and one in the n-p junction in the middle – hence, a dual diode is in fact a three-layer structure. The simulations of the device in previous figures were modeled with three layers of capacitance ($\tilde{C} = [6.67, 15.8, 1.0]$ 0.1 fF/ μm^2), each sandwiched by a layer of resistance ($\tilde{R} = [20, 300, 2000, 25]$ ohms per square) with these parameters based on measured or calculated values. As Fig. 11 shows, when contrasted against a comparable two-layer structure (e.g. ignoring the middle depletion region, equivalent to a p-i-n-i-p device with $\tilde{C} = [6.67, 1.0]$ 0.1 fF/ μm^2 and $\tilde{R} = [20, 300, 25]$ ohms per square), the three-layer simulation exhibits a much sharper response. The gating operation of the simulated two layer structure (22 ps) takes early twice as long as the three layer device (13 ps).

Having the ability to accurately model the voltage behavior across multilayer resistive and capacitive stacks is essential for understanding a stacked diode OCOG. This same analysis method may also be used to help study n-i-p-i devices. Multilayer diffusive conduction analysis has also helped to reveal a useful insight. In analogy with the frequency response of an electrical RC circuit in which the presence of extra RC filters changes the system's filter response (e.g. adding an extra 6 dB/octave per set, modified by the extra load) (Horowitz and Hill 1980), the presence of extra layers significantly speeds up the voltage decay response, although at a cost of reduced voltage swing. This is particularly relevant for diffusive conduction behavior since its hyperbolic decay, although initially fast, slows down considerably at times

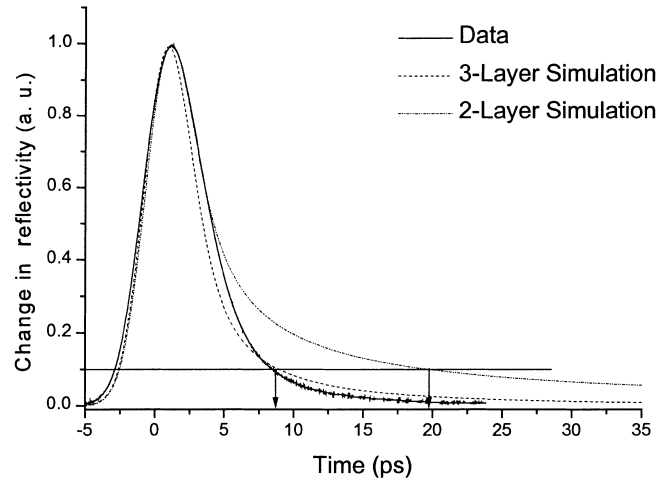


Fig. 11. Small signal response of the OCOG compared to simulations of both three- and two-layer structures. Note the dramatic improvement in the device recovery as the number of layers increases.

large with respect to the diffusion coefficient time constant. The presence of multiple layers provides a method which enables the voltage to drop even more rapidly at the beginning so that by the time the fall-off diminishes, it is significantly lower than it might otherwise have been. The result is not a faster effective diffusion time constant; rather, the response function itself is changed, more closely resembling the multiplication of the individual diffusive conduction decays. As Fig. 11 shows, adding additional layers results in significantly reduced decay times necessary to reach, say, 0.1 or 0.005 of the peak voltage.

7. Conclusions

We have demonstrated a surface-normal, optically controlled optical gate that turns on and off within 20 ps with a 30% reflectivity change, operating with a 20 ps pulse repetition period. A small signal model of voltage behavior across multi-layered structures has been developed and matches the data well, including the intriguing behavior of faster device recovery as the number of layers increases. This device, as it stands, can be potentially switched both faster and with less energy using smaller spot sizes. Future work may include improving processing techniques (particularly that of the ITO), optimizing the RC layers and multiple quantum wells in the structure for larger contrast ratios and faster responses, and fully integrating such structures with a CMOS system via flip-chip bonding.

Acknowledgements

We would like to thank Chris Coldren for growing the tested devices. This work was supported by the US Department of the Army, Army Research Office, grant DAA655-98-1-0160.

Appendix

This section describes in more detail how to determine the coupling diffusion matrix, \tilde{D} , for an arbitrary multilayered structure.

The variables used are shown below in Table 1 and some are illustrated in Fig. 12. Recall that for N (capacitive) layers, there are $N + 1$ resistive planes. Some of the variables are per layer, while others are per resistive plane; care should be taken in relationships involving both N and $N + 1$ indicies.

The N J s are related to the $N + 1$ I s by:

$$\begin{aligned} \frac{dI_1}{dx} &= -J_1 \\ \frac{dI_2}{dx} &= J_1 - J_2 \\ \frac{dI_i}{dx} &= J_{i-1} - J_i \quad \text{for } 1 < i < N + 1 \\ \frac{dI_{N+1}}{dx} &= J_N \end{aligned} \tag{A1}$$

Table 1. Multiple-layer variables

$C_i, i = 1-N$	Capacitance
$V_i, i = 1-N$	Voltage across a layer ('vertical', between resistor planes)
$R_i, i = 1-N + 1$	Resistance
$I_i, i = 1-N + 1$	Current along a resistor plane
$J_i = I_{i+1} - I_i, i = 1-N$	'Vertical' current (current between resistor planes)

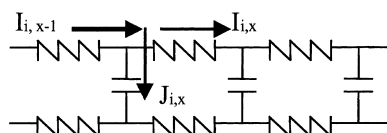


Fig. 12. Illustration depicting I_i and J_i .

This relationship may be rearranged to show the dependence of the J s on the I s:

$$\begin{aligned} J_1 &= -\frac{d}{dx}I_1 \\ J_2 &= -\frac{d}{dx}(-I_1 - I_2) \\ J_i &= -\frac{d}{dx}(-I_1 - I_2 - \dots - I_i) \quad \text{for } i \leq N \end{aligned} \quad (\text{A2})$$

The $(N + 1)$ th equation involving I_{N+1} is simply

$$\frac{d}{dx}I_{N+1} = \sum_{i=1}^N -\frac{d}{dx}I_i \quad (\text{A3})$$

We can rewrite the first $N \times N$ relationship of J in terms of I in matrix notation as shown:

$$\tilde{J}_{[N]} = \frac{d}{dx} \begin{pmatrix} -1 & 0 & 0 & 0 & \dots & 0 \\ -1 & -1 & 0 & 0 & & 0 \\ -1 & -1 & -1 & 0 & & 0 \\ \vdots & & & \ddots & \ddots & \vdots \\ -1 & \dots & & & \dots & -1 \end{pmatrix} \tilde{I}_{[N]} \quad (\text{A4a})$$

or, more succinctly,

$$\tilde{J}_{[N]} = \frac{d}{dx} \tilde{M}_{1[N]}^{-1} \tilde{I}_{[N]} \quad (\text{A4b})$$

where $\tilde{I}_{[N]}$ is a vector of the current along only the first N resistor planes. Note that $\tilde{M}_{1[N]}$ is, similarly, of dimension $N \times N$.

The relationship between the V s and I s is given by

$$\nabla^2 V_i = \frac{d}{dx} I_{i+1} R_{i+1} - \frac{d}{dx} I_i R_i \quad (\text{A5})$$

Again, $(N)V_i$ are described by $(N + 1)I_i$ and R_i . However, we can once more use Equation (A1) to write

$$\nabla^2 V_N = \frac{d}{dx} \left(R_{i+1} \sum_{i=1}^N I_i - R_N I_N \right) \quad (\text{A6})$$

allowing us to use the vector $\tilde{I}_{[N]}$. In matrix form this becomes

$$\nabla^2 \tilde{V} = \begin{pmatrix} -1 & 1 & 0 & \cdots & & & 0 \\ 0 & -1 & 1 & 0 & & & \vdots \\ 0 & 0 & -1 & 1 & & & \\ \vdots & & & & \ddots & & \\ & & & & & \ddots & \\ 0 & 0 & \cdots & 0 & -1 & 1 & 0 \\ \frac{-R_{N+1}}{R_1} & \frac{-R_{N+1}}{R_2} & \cdots & \cdots & \frac{-R_{N+1}}{R_{N-1}} & \frac{-R_{N+1}-R_N}{R_N} & \end{pmatrix} \frac{d}{dx} \tilde{I}_{[N]} \tilde{R}_{[N]} \quad (\text{A7a})$$

or

$$\nabla^2 \tilde{V} = \tilde{M}_{2[N]} x \frac{d}{dx} \tilde{I}_{[N]} \tilde{R}_{[N]} \quad (\text{A7b})$$

where it is understood $\tilde{I}_{[N]} \tilde{R}_{[N]}$ is an element-by-element multiplication, not matrix multiplication. Since $\tilde{M}_{2[N]}$ is an $N \times N$ matrix, finding the inverse of M_2 is straightforward.

Putting it all together, we have three distinct equations:

$$\begin{aligned} \tilde{J}_{[N]} &= \frac{d}{dx} \tilde{M}_{1[N]}^{-1} \tilde{I}_{[N]} \\ \nabla^2 \tilde{V} &= \tilde{M}_{2[N]} \frac{d}{dx} \tilde{I}_{[N]} \tilde{R}_{[N]} \\ \frac{\partial}{\partial t} \tilde{V} &= \frac{\tilde{J}}{\tilde{C}} \end{aligned} \quad (\text{A8})$$

(Equations (A5) and (A2) are reprinted here for clarity) where the multiplication (of \tilde{R}) and division (of \tilde{C}) mean element-by-element operations instead of matrix operations. Combining these three equations, we can solve for the coupling diffusion matrix, \tilde{D} , resulting in Equation (25).

As mentioned earlier, from this point forward the method described in Section 5 for determining the voltage dynamics using eigenvalues and eigenvectors becomes straightforward to apply, providing a complete solution to the voltage dynamics of a multilayer structure.

References

- Ahn, K.H., X.D. Cao, Y. Liang, B.C. Barnett, S. Chaikammerd and M.N. Islam. *J. Opt. Soc. Am. B.* **14** 1228, 1997.
 Aitchison, J.S., A.H. Kean, C.N. Ironside, A. Villeneuve and G.I. Stegeman. *Elec. Lett.* **27** 1709, 1991.
 Bradley, P.J., C. Rigo and A. Stano. *IEEE J. Quantum Elec.* **32** 43, 1996.

- Campi, D., C. Coriasso, A. Stano, L. Fautinno, C. Cacciatore and C. Rigo. *Appl. Phys. Lett.* **72** 537, 1998.
- Dohler, G.H. *IEEE J. Quantum Elec.* **22** 1682, 1986.
- Doran, N.J. and D. Wood. *Opt. Lett.* **13** 56, 1988.
- Eiselt, M. *Elec. Lett.* **28** 1505, 1992.
- Eiselt, M., W. Pieper and H.G. Weber. *J. Lightwave Tech.* **13** 2099, 1995.
- Ellis, A.D. and D.M. Spritir. *Elec. Lett.* **29** 2115, 1993.
- Gontijo, I., D.T. Neilson, A.C. Walker, G.T. Kennedy and W. Sibbett. *IEEE J. Quantum Elec.* **32** 2112, 1996.
- Goossen, K.W., J.A. Walker, L.A. D'asaro, S.P. Hui, B. Tseng, R.E. Leibenguth, D. Kossives, D.D. Bacon, D. Dahringer, L.M.F. Chirovsky, A.L. Lentine and D.A.B. Miller. *IEEE Phot. Tech. Lett.* **7** 360, 1995.
- Gulden, K.H., H. Lin, P. Kiesel, P. Riel and G.H. Dohler, K.J. Ebeling. *Phys. Rev. Lett.* **66** 373, 1991.
- Horowitz, P. and W. Hill. *The Art of Electronics*, Cambridge University Press, England, 1980.
- Islam, M.N. *Opt. Lett.* **14** 1257, 1989.
- Islam, M.N. and C.E. Socoloch. *Opt. Lett.* **6** 1490, 1991.
- Islam, M.N., C.E. Socoloch and D.A.B. Miller. *Opt. Lett.* **15** 909, 1990.
- Islam, M.N., C.E. Socoloch and J.P. Gordon. *Opt. Quantum Elec.* **24** S1215, 1992.
- Kan'an, A.M., P. Likamwa, M. Dutta and J. Pamulapati. *IEEE Phot. Tech. Lett.* **8** 1641, 1996.
- Kobayashi, H., R. Takahashi, Y. Matsuoka and H. Iwamura. *Elec. Lett.* **34** 908, 1998.
- Lentine, A.L. and D.A.B. Miller. *IEEE J. Quantum Elec.* **29** 655, 1993.
- Leuthold, J., P.A. Besse, E. Gamper, M. Dulk, St. Fischer and H. Melchior. *Elec. Lett.* **34** 1598, 1998.
- Likamwa, P., A. Miller, C.B. Park, J.S. Roberts and P.N. Robson. *Appl. Phys. Lett.* **57** 1846, 1990.
- Likamwa, P., P.N. Robson, J.P.R. David, G. Hill, P. Mistry, M.A. Pate and J.S. Roberts. *Elec. Lett.* **22** 1129, 1986.
- Livescu, G., D.A.B. Miller, T. Sizer, D.J. Burrows, J. Cunningham, A.C. Gossard and J.H. English. *Appl. Phys. Lett.* **54** 748, 1989.
- Loka, H.S. and P.W.E. Smith, *IEEE J. Quantum Elec.* **36** 100, 2000.
- Mannin, R.J., A.D. Ellis, A.J. Poustie and K.J. Blow. *J. Opt. Soc. Am. B* **14** 3204, 1997.
- Miller, D.A.B. *Opt. Quantum Elec.* **22** S61, 1990.
- Miller, D.A.B., D.S. Chemla, T.C. Damen, A.C. Gossard, W. Wiegmann, T.H. Wood and C.A. Burrus. *Phys. Rev. B* **34** 1043, 1985.
- Parameswaran, K.R., M. Fujimura, M.H. Chou and M.M. Fejer. *IEEE Phot. Tech. Lett.* **12** (2000), in press.
- Paye, J. and D. Hulin. *Appl. Phys. Lett.* **62** 1326, 1993.
- Poole, P.J., C.C. Phillips, M. Henini and O.H. Hughes. *Semicond. Sci. Technol.* **8** 1750, 1993.
- Schneider, H., E.C. Larkins, J.D. Ralston, J. Fleissner, G. Bender and P. Kidl. *Appl. Phys. Lett.* **60** 2648, 1992.
- Sololoff, J.P., P.R. Prucnal, I. Glesk and M. Kane. *IEEE Phot. Tech. Lett.* **5** 787, 1993.
- Stegeman, G.I. and A. Miller. In: *Photonics in Switching, J.E. Midwinter, ed.* Vol. 1, Chapter 6. Academic Press, San Diego, 1993.
- Streb, D., M. Vitzethum, P. Kiesel, G.H. Dohler and M. Kneissl. *Superlattices and Microstruct.* **25** 21, 1999.
- Takahashi, R., Y. Kawamura and H. Iwamura. *Appl. Phys. Lett.* **68** 153, 1996.
- Yairi, M.B., C.W. Coldren, D.A.B. Miller and J.S. Harris, Jr. *Appl. Phys. Lett.* **75** 597, 1999.
- Yairi, M.B., H.V. Demir, C.W. Coldren, D.A.B. Miller and J.S. Harris, Jr. *IEEE LEOS 1999 Annual Meeting*, Paper ThN2, 770, 1999.
- Yang, C.M., E. Canoglu, E. Garmire, K.W. Goossen, J.E. Cunningham and W.Y. Jan. *IEEE J. Quantum Elec.* **33** 1498, 1997.
- Yokohama, I., M. Asobe, A. Yokoo, H. Itoh and T. Kaino. *J. Opt. Soc. Am. B* **14** 3368, 1997.